Article

Not peer-reviewed version

Topology Optimization and Efficiency Evaluation of Short-Fiber Reinforced Composite Structures considering Anisotropy

Evgenii Kurkin * , Oscar Ulises Espinosa Barcenas , Evgenii Kishov , Oleg Lukyanov

Posted Date: 13 December 2023

doi: 10.20944/preprints202312.0789.v1

Keywords: multidisciplinary analysis and optimization; topology optimization; anisotropy; short fibers reinforced composites doi:10.20944/preprints202312.0789.v1

Article

Topology Optimization and Efficiency Evaluation of Short-Fiber Reinforced Composite Structures Considering Anisotropy

Evgenii Kurkin *, Oscar Ulises Espinosa Barcenas, Evgenii Kishov and Oleg Lukyanov

Department of Aircraft Construction and Design, Samara National Research University, 34 Moskovskoe Shosse, Samara 443086, Russia; evgeniy.kishov@ssau.ru (E.Ki.), lukyanov.oe@ssau.ru (O.L.), oscar.espinosa.barcenas@hotmail.com (O.U.E.B.)
* Correspondence: kurkin.ei@ssau.ru; Tel.: +7-960-831-9009

Abstract: The current study aims to develop a methodology for obtaining topology-optimal structures made of short fiber-reinforced polymers, which include the fluid-structure interaction. Accounting for the molding process during the internal iterations of topology optimization makes it possible to enhance the weight efficiency of structures—a crucial aspect, especially in aerospace. Anisotropy is considered through the fiber orientation tensor, which is modeled by solving the plastic molding equations for non-Newtonian fluids, and then introduced as a variable of the stiffness matrix during the structural analysis. The materials used were non-linearly modeled using an exponential-and-linear hardening law. The evaluation of weight efficiency in structures composed of short-reinforced composite materials using a dimensionless criterion is addressed. Experimental verification was performed to confirm the validity of the developed methodology. The evidence illustrates that considering anisotropy leads to stiffer structures and structural elements should be oriented in the direction of maximal stiffness. The load-carrying factor can be expressed in terms of failure criteria. The presented multidisciplinary methodology can be used to improve the quality of the design of structures made of short fiber-reinforced composites (SFRC) where high stiffness, high strength, and minimum mass are the primary required structural characteristics.

Keywords: multidisciplinary analysis and optimization; topology optimization; anisotropy; short fibers reinforced composites

---

1. Introduction

The aerospace and automotive industries have inherent requirements: high stiffness, high strength, and minimum mass are the primary concerns when designing structures [1–4]. For instance, high stiffness and minimal mass are required to limit the natural frequency of spacecraft to avoid resonance between the launch vehicle and itself [4–6], and in automobiles to improve performance while satisfying safety requirements [7–9]. Minimal mass is required for keeping the spacecraft structure lightweight to get to the desired orbital altitude by increasing the useful load fraction [10], lowering aircraft engineering costs by reducing airframe weight [11,12], and reducing aircraft and automobile operational costs by increasing fuel efficiency [11–13]. High strength is linked to the minimal mass requirement since materials with higher specific strength allow to keep mass to a minimum. The same applies to the high stiffness requirement by using materials with high specific stiffness.

The strength of the structure depends on the structure's shape and material. Regarding materials, aluminum and titanium [14] are commonly used in the aerospace and automobile industries due to their high specific strength and stiffness. Moreover, new materials have been researched for automobile [15] and aerospace applications [16–19], including ceramics [20], composites [21], and nanocomposites [22]. Furthermore, nanocomposites [23,24], shape memory polymers [25,26], and short fiber-reinforced composites (SFRC) have experienced an increase in aerospace applications in recent years [20,27–33]. The principal metrics for comparing materials, rather than Young's modulus or the ultimate tensile strength, are the specific stiffness and strength as both mechanical characteristics are normalized by material density. Current strategies for designing efficient structures can be categorized into guidelines and recommendations [34,35], methods and methodologies [36–38], and even parametric [39–41] and topology optimizations [40,42–47]. Topology optimization (TO) has proven to be an excellent mathematical method for designing efficient structures and optimizing material arrangement within a given design space for a set of loads, boundary conditions, and constraints with the goal of minimizing a specific objective function. This method, also known as the variable density model, was originally proposed in the work [48], where it was applied to the optimal design of two-dimensional structures to overcome the computational difficulties associated with stress analysis of variable thickness plates. Three-dimensional (3D) TO under strength and stiffness constraints, using material density as a design variable, was later presented in the studies [49–51]. Another approach to representing variable density using materials at the microstructure level and its application to TO problems can be found in the study [52], further explained in the work [53]. Designed structures are usually evaluated by considering maximum displacement, maximum strength, failure criteria values [54–56], or minimum mass of the structure, which are not reliable indicators since these values are local, except for mass, which is evaluated as an integral characteristic and does not provide comprehensive information about the structure other than its value. However, the load-carrying factor LCF G, proposed by Andrey Komarov in 1965 [48], allows us to relate both structural efficiency and weight requirements, facilitating objective comparisons between structures with relatively low levels of computational and modeling effort [57]. The fundamental physical meaning of the load-carrying factor is the integral characteristic of the structure, reflecting the internal forces in its elements (the mode of action of an external force on a structure up to its supports) and the extent of these internal forces (the extent of the external forces transmission paths). A disadvantage of the LCF is its dimensional dependence; if the geometrical dimensions of the structure and external loads are changed, the magnitude of the LCF also changes, making it difficult to compare different structural arrangements. Therefore, the usage of the LCF coefficient, as proposed by Valery Komarov in the work [58], is more appropriate. In the accompanying article [59], a proposal is made to employ the method of mixtures for assessing the weight efficiency of composite structures, necessitating a detailed examination of composite materials at the microstructure level. From a practical standpoint, the utilization of strength criteria at the representative volume mesolevel appears to be more advantageous when evaluating complex-shaped structures for weight efficiency. In the present work, the strength criterion for homogenized composite material will be considered.

In summary, current modern materials such as SFRC, TO, metrics for assessing the structure shape as failure criteria, and LCF have contributed to increase stiffness and strength while reducing the mass of structures. However, the interaction between them is often not carefully considered. The fiber orientation tensor is obtained by means of solving the Folgar-Tucker's continuity equation, which is developed based on the fiber orientation kinetic theory of fiber suspensions [60–63]. SFRC is modelled as transversely isotropic material, even though its stiffness depends not only on the material's mechanical characteristics but also on the fiber orientation tensor [64]; TO is typically performed in an isotropic medium [65,66], and LCF accounts for the equivalent stress of structures made of isotropic materials. In other words, anisotropy is either partially or completely ignored at various stages of the design process.

This work aims to develop a methodology for obtaining topology-optimal structures made of SFRC. The objectives of this work are as follows: to make the stiffness matrix dependent on the fiber orientation tensor, to obtain the fiber orientation tensor by performing injection molding simulations, to formulate a metric for assessing SFRC structures that simultaneously evaluates the shape and material of the structure, and to experimentally verify the developed methodology. It is assumed that by considering the anisotropy during TO, the resulting topology will perform better than a topology obtained in an isotropic medium. Moreover, the anisotropy is directly related to the arrangement of fibers within the structure, specifically to the fiber orientation tensor, which is obtained by solving Folgar-Tucker's continuity equation [67] through modeling the injection molding process within the designated design region in Autodesk Moldflow. The consideration of anisotropy induced by the fiber arrangement is achieved by implementing the Advani-Tucker orientation averaging procedure on the material stiffness matrix [68] and attaching the resultant tensor to each mesh element. This procedure was realized with AnisoTopo [69]. The attachment of the stiffness matrix was accomplished by interpolating the meshes of the injection and structural models with Digimat MAP. Finally, TO was performed without altering the stiffness arrangement within the design region. The resultant topology can be assessed using a metric such as a modified LCF, which is described in terms of failure criteria for composite materials, such as the Tsai-Hill failure criterion.

The numerical and experimental results of this study confirm that considering the anisotropy during TO increases the stiffness of the resultant topologies. This is achieved by obtaining the fiber orientation tensor by solving the Navier-Stokes equations for non-Newtonian fluids and making the stiffness matrix dependent on the obtained fiber orientation tensor.

2. Materials and Methods

2.1. Materials and material models

Three different materials and their non-linear models were considered (see Figure 1 and Table 1). These materials include two anisotropic materials: a 50% glass fiber reinforced polyamide 6, denoted as PA6 50GF [70], along with its associated model as presented in [71], and a 30% carbon fiber reinforced polyamide 6, referred to as PA6 30CF [72] with its corresponding model [73]. Additionally, an isotropic material, the D16T aluminum alloy [74], which shares similarities with the 2024 -T4 ASTM aluminum alloy. It's worth noting that no specific preparation steps or treatments were applied to these materials before testing. Mechanical characteristics of these materials were determined through tensile tests conducted on samples cut from injected-molded plates with dimensions 200 x 150 x 4 mm, following ISO 527-2:2012(en) standard [75]. While the primary mechanical characteristics relevant to this study are summarized in Table 1, more comprehensive details on the material characteristics can be found in their respective documentation.

The material models for PA6 50GF and PA6 30GF were calibrated with experimental data as described in [73]. In summary, this calibration method involves modeling the material microstructure as a two-phase material and taking into account the fiber orientation in the calculation of mechanical properties. The material's mechanical properties were obtained by homogenizing the fibers and matrix using a second-order Mori–Tanaka homogenization scheme in Digimat MF. As the mechanical properties correspond to a unidirectional fiber-reinforced composite, it is modeled as a transversely isotropic material. Accounting for the fiber orientation was achieved by applying Tucker's averaging procedure. The matrix stress–strain state is described using the J2 plasticity model based on von Mises' equivalent stress. When the equivalent stress σ_{eq} exceeds the yield stress σ_y, the reaction becomes nonlinear, and plastic deformation occurs. The plastic strength is then defined as

$$\sigma_{plastic} = \sigma_y + R(\varepsilon_p), \qquad (1)$$

where σ_y is the yield stress; $R(\varepsilon_p)=k\varepsilon_p + R_\infty[1 - e^{-m\varepsilon_p}]$ represents the isotropic strain exponential and linear hardening law, and ε_p is the accumulated plastic strain. Here, k is the linear hardening modulus in MPa; m is the hardening exponent; and R_∞ is the hardening modulus, MPa. The material model parameters were adjusted by minimizing the difference between the tensile strain-stress curves of the composite material and the experimental results.

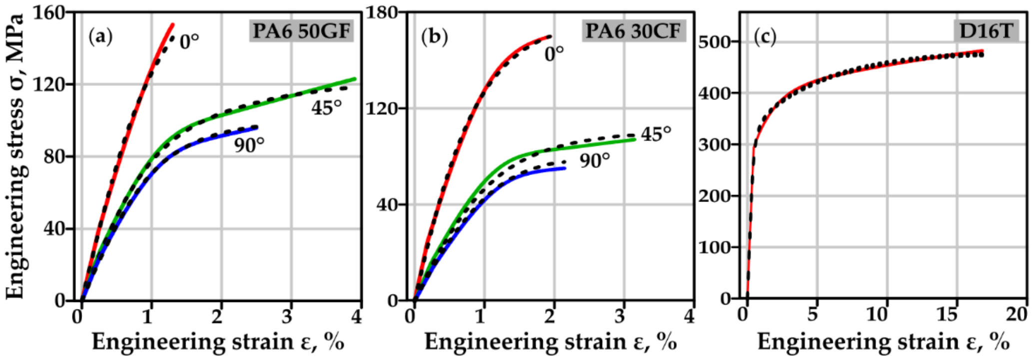

Figure 1. Stress-strain curve: (**a**) PA6 50GF; (**b**) PA6 30CF; (**c**) D16T. Solid lines - model, dashed line - experiment. Angle between polymer flow and tension load: 0° - red, 45° - green, 90° - blue.

Table 1. Material characteristics and mechanical properties.

Characteristics	**Material**		
	PA 50GF	**PA 30CF**	**D16T**
Matrix phase			
Matrix density, kg/m³	1148		2770
Young's modulus, E_m (MPa)	4911	3994	66059
Poisson's coefficient, υ_m	0.372	0.372	0.330
Yield stress, σ_y (MPa)	17.21	14.5	294.48
Hardening modulus, R_∞ (MPa)	37.1	37.00	109.51
Hardening exponent, m	371.21	458.30	75.72
Linear hardening modulus, k (MPa)	313.02	188.40	1107.60
Reinforcement phase			
Fiber density, kg/m³	2550	1780	-
Young's modulus, E_f (MPa)	72000	230000	-
Poisson's coefficient, υ_f	0.22	0.20	-
Fibers', AR	13.58	16.54	-
Wt. %	30	50	-
Material ultimate tensile strength			
Longitudinal, X (MPa)	153.31	169.35	476
Transverse, Y (MPa)	97.82	85.07	-
Transverse shear strength, S (MPa)	83.90	66.33	-

2.2. Methods

2.2.1 Topology optimization

Topology optimization (TO) represents an effective approach for optimizing material distribution within a structure to enhance the transfer of internal forces from areas of load-carrying areas to support regions. Since the strain energy quantifies the energy stored in a body due to deformation, minimizing this response leads to a reduction in the body's compliance [51]. Strain energy is mathematically defined as W = 0.5 Fu, where F = Ku is the force expressed as the product of the stiffness K and deformation u. The stiffness is influenced by anisotropy resulting from the arrangement of fibers within the body, specifically the fiber orientation tensor.

In this study, the objective function of TO was to minimize the structure compliance by reducing the total strain energy of an anisotropic composite material. This was achieved by adjusting the topology density ρ within the design region Ω while adhering to the given design region volume to retain $g_1(\mathbf{x})$ and constraints such as the "Member size" and the "Pull-out direction". The formulation was defined as follows:

$$\begin{aligned}
&\text{minimize} && f(\mathbf{x}) = 0.5\mathbf{u}^T\mathbf{K}(\varrho(\mathbf{x}), \mathbf{A}(\mathbf{x}))\mathbf{u},\\
&\text{by varying} && \mathbf{x} \in \boldsymbol{\Omega},\\
&\text{subject to} && h(\mathbf{x}) = \mathbf{K}(\varrho(\mathbf{x}), \mathbf{A}(\mathbf{x}))\mathbf{u} - \mathbf{F} = 0,\\
& && g_1(\mathbf{x}) = \int \varrho(\mathbf{x})d\Omega - V_{ret} \leq 0,\\
& && g_2(\mathbf{x}) = \varrho(\mathbf{x}) > 0,\\
& && g_3(\mathbf{x}) = \varrho(\mathbf{x}) \leq 1,\\
& && g_4(\mathbf{x}) = \int |\nabla\varrho(\mathbf{x})| d\Omega - \quad \delta \leq 0,\\
& && g_5(\mathbf{x}) = \varrho_i - \varrho_k \leq 0 \qquad \forall\ x_i = x_k,\ y_i = y_k,\ |z_i| \geq |z_k|,
\end{aligned}$$

Here, **K** represents the global stiffness matrix, **u** denotes the nodal displacement vector, F is the nodal force vector, and **x** is the vector containing design domain elements with coordinates x, y, z. **A** represents the fiber orientation tensor, and δ is related to the minimum structural member size. TO, in this work, was performed using the "Sequential Convex Programming" solver within the Ansys Mechanical Workbench software.

2.2.1.1 Unidisciplinary topology optimization considering constant anisotropy

Anisotropy was modeled by adjusting the elastic constants of the stiffness matrix. Since composites reinforced with 30–50 wt.% fiber along the flow direction exhibit double the stiffness compared to that across the flow direction [76], the anisotropy was incorporated by modifying stiffness matrix components. The mechanical characteristics of the anisotropic material were aligned with the global coordinate axis and remained constant throughout the TO, allowing for the optimization of structure arrangement based on a predefined stiffness distribution.

2.2.1.2 Multidisciplinary topology optimization considering variable anisotropy

As explained in the previous section, modeling the anisotropy during structural analysis involves incorporating the relevant material characteristics of an anisotropic material. However, this approach is suitable for cutting structures from injection-molded plates (two-dimensionally) but not for molded structures (three-dimensionally). In molded structures, the fiber orientation within the channels, which are structural elements from the perspective of solid mechanics, cannot be defined until TO is performed.

The technique outlined in [76] was applied to account for fiber arrangement within the channels and dynamically adjust the mechanical characteristics of each structural element by recalculating the element's fiber orientation tensor. Algorithm 1 presents the pseudocode for multidisciplinary TO considering variable anisotropy, with detailed information on files and program execution available in [77].

The process begins with the introduction of initial values, including boundary conditions for structural analysis $\boldsymbol{BC_{struct}}$ and injection molding simulation $\boldsymbol{BC_{injMold}}$, material properties of the matrix and fiber $\boldsymbol{MP_{matrix+fiber}}$, injection molding material $\boldsymbol{MP_{injMold}}$, TO parameters $\boldsymbol{OP_{topoOpt}}$, topology density threshold th, design region volume percentage to retain V_{ret}, interpolation tolerance between the injection molding and structural analysis meshes δ_{map}, and an optional *geo.stp* file for geometry. $\boldsymbol{MP_{matrix+fiber}}$ and $\boldsymbol{OP_{topoOpt}}$ are saved as materialProperties.txt and topoParameters.txt, respectively, for correct utilization in AnisoTopo [69]. The structural domain region mesh, elements participating in TO, and elements related to boundary conditions are obtained from Ansys Workbench and saved as designRegionMesh.ans, design.txt, and frozen.txt, respectively. TO with variable fiber orientation proceeds after specifying the convergence criterion for TO algorithm, which is the relative difference ε between the previous and current objective function value, not exceeding the objective relative difference ε_{obj}. Key moments in TO include:

First, the structural mesh is exported to Autodesk Moldflow. If it's the first iteration, reducedMesh.ans will be the same as designRegionMesh.ans as it hasn't been previously reduced. Otherwise, the structural mesh is reduced using the "delete_elements" algorithm and saved as reducedMesh.ans (details in [77]).

Second, the reducedMesh.ans, $\boldsymbol{BC_{injMold}}$, and $\boldsymbol{MP_{injMold}}$ are introduced to Moldflow for calculating the fiber orientation tensor **A**, which is exported along with the injection molding mesh $\text{mesh}_{\text{injMold}}$ and saved in the file meshMoldFlow.pat and fiberOrientMoldFlow.xml, respectively. Fiber orientation mapping from injection molding to structural analysis mesh is performed in DigimatMAP, and the mapped fiber orientation **A'** is stored in the file fiberOrientAnsys.xml.

Third, in AnisoTopo [69], **A'** is introduced to calculate the anisotropic stiffness matrix (K) using the Advani-Tucker orientation averaging technique applied to the material stiffness matrix [4]. AnisoTopo's code employs the Mori-Tanaka homogenization method to compute mechanical properties.

The composite strain and stress are contingent on the strain and stress of both the matrix and fiber in proportion to their volume fractions:

$$\varepsilon = (1 - \phi_f)\varepsilon_m + \phi_f\varepsilon_f,$$

$$\sigma = (1 - \phi_f)\sigma_m + \phi_f\sigma_f,$$

where ϕ_f is the fiber volume fraction, and the subscripts m denote the strain and stress of matrix values, while the subscripts f correspond with the strain and stress of the fiber.

The unidirectional short-fiber reinforced composite material is modeled as transversely isotropic. The elastic moduli, as introduced by Tandon and Weng [78], were used to calculate the elastic coefficients:

$$\frac{E_{11}}{E_m} = \frac{1}{1 + \frac{\phi_f(A_1 + 2v_m A_2)}{A_6}}$$

$$\frac{E_{22}}{E_m} = \frac{1}{1 + \dfrac{\phi_f[-2\upsilon_m A_3 + (1-\upsilon_m)A_4 + (1+\upsilon_m)A_5 A_6]}{2A_6}},$$

where E_m, υ_m are the Young's modulus and Poisson ratio of the matrix, respectively. The parameters A_i are the functions of Eshelby's tensor and can be found in [79]. In this particular study, we empoly Eshelby's tensor for an elliptical inclusion, which depends on the fiber's aspect ratio. The Tucker's averaging procedure is used to account for the fiber orientation tensor, described as follows:

$$C_{ijkl} = B_1 a_{ijkl} + B_2(a_{ij}\delta_{kl} + \delta_{ij}a_{kl}) + B_3(a_{ik}\delta_{jl} + a_{il}\delta_{jk} + a_{jl}\delta_{ik} + a_{jk}\delta_{il})$$

$$+B_4(\delta_{ij}\delta_{kl}) + B_5(\delta_{ik}\delta_{jl} + \delta_{il}\delta_{jl}),$$

where a_{ijkl} is the fourth-order fiber orientation tensor, δ_{ij} is the second-order unit tensor, and the coefficients B are related to the components of the stiffness matrix of the transversely isotropic unidirectional composite [80]. This resulting tensor is linked to each mesh element and is exported as apdl_pre.txt to Ansys Mechanical Workbench.

Fourth, the structural analysis is carried out. In all iterations but the first, the structural analysis is performed on the current topology determined by the topology density ρ (details in [76]). Subsequently, ε is calculated, and the topology is extracted based on V_{def} and exported as density.topo. If the current ε is less than ε_{obj} for the number of times specified by the k-iterations criterion K_ε [81] (in this work, three times in a row), TO is stopped, and the last topology is exported as topoOptStruct.stl. Otherwise, the counter g is incremented by 1, and the loop repeats until convergence is achieved.

Algorithm 1. Multidisciplinary topology optimization.

```
Input: $BC_{struct}$, $BC_{injMold}$, $MP_{injMold}$, $MP_{matrix+fiber}$, $OP_{topoOpt}$, th, $\delta_{map}$, $V_{def}$, $\varepsilon_{obj}$, geo.stp (Optional)
Output: topoOptStruct.stl
write materialProperties.txt ← $MP_{fiber+matrix}$
write topoParameters.txt ← $OP_{topoOpt}$
$mesh_{struct}$, $design_{elements}$, $frozen_{elements}$ = AnsysWorkbench_Mesh($BC_{struct}$, geo.stp);
write designRegionMesh.ans ← $mesh_{struct}$, design.txt ← $design_{elements}$, frozen.txt ← $frozen_{elements}$;
g = 1;
counter_epsilon = 0;
while (counter_epsilon < $K_\varepsilon$) do
    if g == 1 then
        reducedMesh.ans = designRegionMesh.ans;
    else
        domain_mesh_reduced = delete_elements(designRegionMesh.ans, th, $(density.txt)_{g-1}$);
        write reducedMesh.ans ← domain_mesh_reduced
    end if
    $mesh_{injMold}$, A = AutodeskMoldFlow(reducedMesh.ans, $BC_{injMold}$, $MP_{injMold}$);
    write meshMoldFlow.pat ← $mesh_{injMold}$, fiberOrientMoldFlow.xml ← A;
    A' = DigimatMAP(fiberOrientMoldFlow.xml, meshMoldFlow.pat, designRegionMesh.ans, δ);
    write fiberOrientAnsys.xml ← A';
    $K_{EL}$ = AnisoTopo(materialProperties.txt, fiberOrientAnsys.xml, topoPararmeters.txt, designRegionMesh.ans, design.txt, frozen.txt);
    write apdl_pre.txt ← $K_{EL}$;
    if g == 1 then
```

```
                $W_g$ = AnsysWorkbench_StructuralAnalysis(designRegionMesh.ans, apdl_pre.txt, $BC_{struct}$);
            else
                $W_g$ = AnsysWorkbench_StructuralAnalysis(designRegionMesh.ans, apdl_pre.txt, $BC_{struct}$, $\rho$);
                $\varepsilon_g = |(W_g - W_{g-1})/W_{g-1}|$
                if $\varepsilon_g <= \varepsilon_{obj}$ then
                    counter_epsilon ++
                else
                    counter_epsilon = 0
                end if
            end if
            $\rho$ = AnsysWorkbench_TopologyOptimization_Iteration(designRegionMesh.ans, design.txt, frozen.txt, $V_{def}$, topoPara, apdl_pre.txt, $W_g$)
            write density.topo ← $\rho$;
            Convert density.topo to $(\text{density.txt})_g$ with HDFView();
            g++
        end while
        topoOptStruct = delete_elements(designRegionMesh.ans, th, $(\text{density.txt})_{g-1}$);
        write topoOptStruct.stl ← topoOptStruct
```

2.2.2 Metric for evaluating structure design quality of composite materials

The load-carrying factor (LCF), denoted as G, along with its coefficient C_K, is employed to assess the quality of a structural arrangement [57,58]. Their typical formulations are defined as follows:

$$G = \int_V \sigma_{eq}\, dV, \tag{2}$$

$$C_K = \frac{G}{Fl} \tag{3}$$

Here, σ_{eq} represents the equivalent stress, V is the volume of the structure, F is the characteristic load in N, and l is the characteristic linear dimension in m (l represents the distance between areas where loads are applied to the locations of the supports). To properly evaluate the quality of the structural arrangement in composite materials, the LCF has been redefined based on stress criteria.

For structures made of isotropic materials, the LCF is expressed as

$$G = \sigma^{UTS} \int_V F_{eq}\, dV, \tag{4}$$

Here, σ^{UTS} is the ultimate tensile stress, $F_{eq} = \sigma_V / \sigma^{UTS}$ is the maximum stress criterion, defined as the ratio of von Mises stress σ_V to the material's ultimate tensile stress σ^{UTS}. The LCF coefficient remains the same as in Equation 3.

In the case of structures made of anisotropic materials, the LCF is expressed as

$$G_{TH} = \sigma_0^{UTS} \int_V F_{TH}\, dV, \tag{5}$$

Here, σ_0^{UTS} is the ultimate tensile strength either along the longitudinal direction (along the fiber), and F_{TH} is the average Tsai-Hill criterion, determined using Advani-Tucker's averaging procedure [68]. It is defined as follows:

$$\begin{aligned} F_{TH} = {} & E_1 a_{ijkl} + E_2\left(a_{ij}\delta_{kl} + a_{kl}\delta_{ij}\right) + E_3\left(a_{ik}\delta_{jl} + a_{il}\delta_{jk} + a_{jl}\delta_{ik} + a_{jk}\delta_{il}\right) + E_4\left(\delta_{ij}\delta_{kl}\right) \\ & + E_5\left(\delta_{ik}\delta_{jl} + \delta_{il}\delta_{jk}\right), \end{aligned} \tag{6}$$

where $E_1 = F_{1111}^{ud} - 2\,F_{1122}^{ud} + F_{2233}^{ud} - 4\,F_{1212}^{ud} + F_{2323}^{ud}$; $E_2 = F_{1122}^{ud} - F_{2233}^{ud}$; $E_3 = F_{1212}^{ud} - F_{2323}^{ud}$; $E_4 = F_{2233}^{ud}$; $E_5 = F_{2323}^{ud}$. The values of the Tsai-Hill criteria tensor are determined using the following expression:

$$F_{TH}^{ud} = \frac{\sigma_{11}^2}{X^2} - \frac{\sigma_{11}(\sigma_{22}+\sigma_{33})}{X^2} + \frac{\sigma_{22}^2+\sigma_{33}^2}{Y^2} + \left(\frac{1}{X^2}-\frac{1}{Y^2}\right)\sigma_{22}\sigma_{33} + \frac{\sigma_{12}^2+\sigma_{13}^2}{S^2} + \left(\frac{4}{Y^2}-\frac{1}{X^2}\right)\sigma_{23}^2, \quad (7)$$

Here, σ_{ij} represents the components of the stress tensor (component 11 corresponds to the fiber's longitudinal axis, etc.), X is the longitudinal strength limit, Y is the transverse strength limit, S is the transverse shear strength. The LCF coefficient, accounting for the anisotropy, can be written as

$$C_K^{TH} = \frac{G_{TH}}{Fl} \quad (8)$$

2.2.3 Brackets manufacturing and load testing technique

The two- and three-dimensional brackets were manufactured by injection molding using a Negri Bossi VE 210-1700 injection molding machine. The filling parameters were as follows: melt temperature 230 °C, mold temperature 80 °C. The pellets were dried before the injection at a temperature of 90 C for 4 h in a plastic pellet dryer. The two-dimensional brackets were cut from the injected molded plates, while the three-dimensional brackets were molded. Mold for three-dimensional brackets injection molding was manufactured from St-3 steel plates underwent CNC machining using a 4-flute 4 mm AlTiN D4x50x4Dx4F coated carbide endmill.

A static test was conducted to verify the developed methodology on both brackets. Before conducting the static test, the brackets were weighed using an electronic balance with a resolution of 0.01 g. Both brackets are loaded along the Y-axis until they fail. Restricting plates were used to ensure that the brackets failed due to fracture and not by buckling.

The mechanical testing equipment for both brackets consisted of an MTS 322 testing machine with mechanical grips, an MTS 793 controller, and an MTS 661.20F-03 force sensor, as well as special equipment shown in Figure 2, which included auxiliary rods and plates. Before performing the tensile test, the bracket support 1 and loading rod 2 were positioned. A mounting tool was used to check the collinearity between the bracket's support and loading rod axes, and a construction level was used to ensure the vertical straightness of the loading scheme. Subsequently, the bracket was positioned between the bracket support plates and secured with M6 bolts. Displacement-restricting plates 3 were attached to the bracket support 1 using M6 bolts. Linking rod 4 is attached to the loading rod 1 with M6 bolts. The alignment of the bracket and linking-rod axes was achieved by adjusting the height of the loading rod. Finally, the bracket and linking rod were fixed in place using M6 bolts. After positioning all the components and ensuring that the bracket was not pre-stressed, the gauge sensor was set to zero.

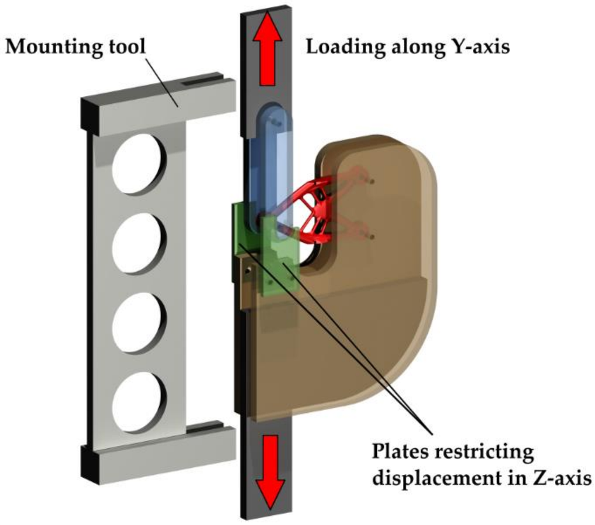

Figure 2. Loading scheme of and special mechanical testing equipment for bracket testing.

3. Results

TO was performed on two case studies to obtain the structural layout in two- and three-dimensional spaces. In the two-dimensional case, the topologies obtained with and without considering constant anisotropy were compared. In the three-dimensional case, the solutions obtained using fixed and variable fiber orientation were compared. The materials used were PA6 50GF, PA6 30CF, and D16T. The aluminum structures, along with the LCF coefficient, serve as a control for comparing the resultant topologies.

3.1. Topology optimal two-dimensional structures

3.1.1. Topology optimization and structural arrangement quality assessment

In the two-dimensional case, the design space is a rectangle with dimensions 75 x 50 x 4 mm, as shown in Figure 3, where frozen elements near the loads and supports are marked in grey. The structured mesh consists of 47862 elements, with an edge size of 0.25 mm. This was assessed by element quality mesh metric, with a minimal value of 0.4009, a maximum value of 0.9949, an average value of 0.8834, and a standard deviation of 6.4556 x 10^{-2}.

The force F was applied to the elements located within the ring at the center-right side of the region, while the displacement on the elements within the rings on the left side was set to 0 mm. The design region volume percentage to retain m_{ret} was set to 12%. The objective relative difference ε_{obj} value was established as 0.1%. The material properties were defined as follows: for isotropic material - Young's modulus of 8 GPa and a Poisson's ratio of 0.25; for orthotropic material - the following elastic constants $E_X = 13$ GPa, $E_Y = 7$ GPa, $E_Z = 6.5$ GPa, $\upsilon_{XY} = 0.272$, $\upsilon_{YZ} = 0.365$, $\upsilon_{XZ} = 0.254$, $G_{XY} = 1.979$ GPa, $G_{YZ} = 1.639$ GPa, $G_{XZ} = 1.763$ GPa (the X-axis correspond to the bracket symmetry axis, the Y-axis corresponds to force direction, the Z axis is determined by the right-hand rule).

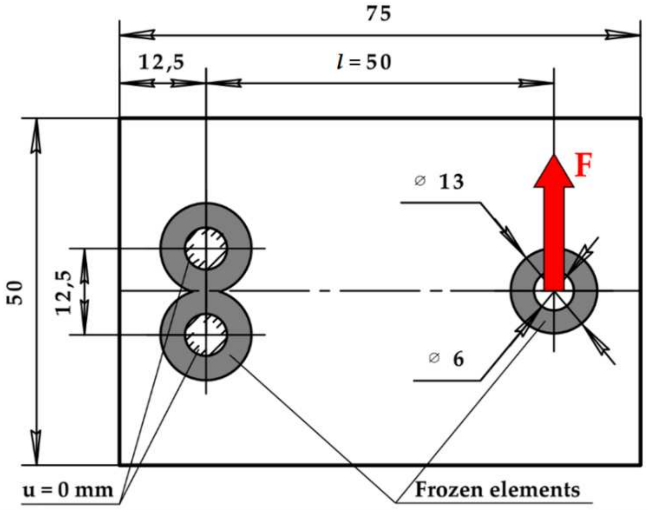

Figure 3. Topology optimization design region, boundary conditions and load case.

The convergence results are plotted in Figure 4. A converged solution was achieved after 44 and 34 iterations for TCA (Topology Constant Anisotropy) and TCI (Topology Constant Isotropy) cases, respectively. The resultant topologies are shown in Figure 5; the topology considering isotropy and constant anisotropy will be further referred to as TCI and TCA, respectively (where C stands for constant, even though isotropy is constant by definition).

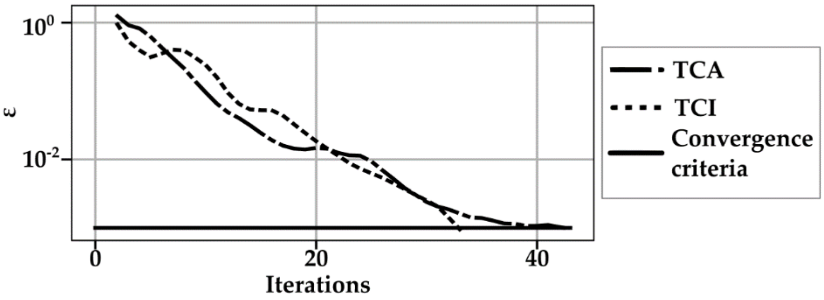

Figure 4. Topology optimization convergence plot by total strain energy relative error.

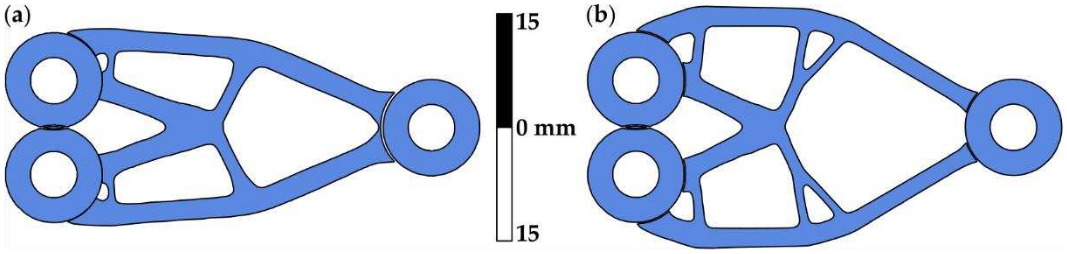

Figure 5. Resultant two-dimensional structures: (**a**) TCA; (**b**) TCI.

The von Mises-based and Tsai-Hill failure criterion fields of the resultant two-dimensional topologies, loaded at a force corresponding to the relation $^F/_m$ =70 N/gr, are presented in Figure 6. It can be observed that the von Mises failure criterion underestimates the strength of structural members loaded transverse to the fiber direction. Meanwhile, the Tsai-Hill failure criterion allows for a more accurate estimation of the strength of structures made of short-reinforced composite materials.

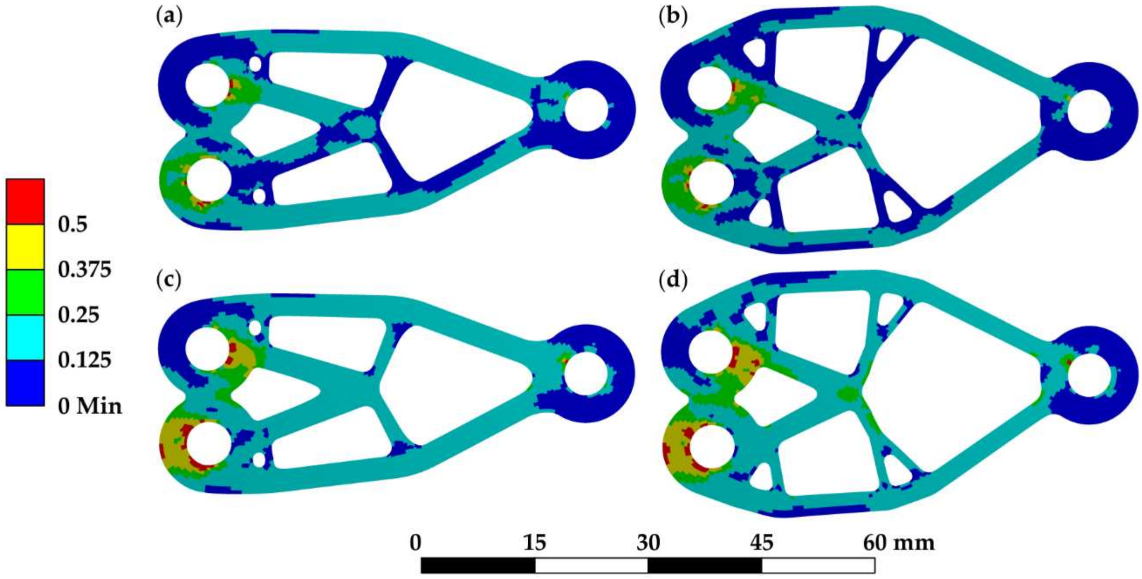

Figure 6. Failure criteria field of two-dimensional topologies: (a) von Mises-based failure criterion field of TCA; (b) von Mises-based failure criterion field of TCI; (c) Tsai-Hill failure criterion field of TCA; (d) Tsai-Hill failure criterion field of TCI.

The failure criteria and volume of each element in equations (3) and (7) were multiplied and summed to calculate the LCF and LCF coefficients. The LCF and LCF coefficient of each topology and failure criterion combination are presented in Table 2. The relative percentage difference was calculated between the LCF coefficients of TCA and TCI.

Table 2. LCF coefficient baseline and reconstructed TCA and TCI.

Topology	m, g	f, N	C_K	C_K^{TH}
		PA6 50GF		
TCA	4.655	326.8	5.2928	5.6994
TCI	4.658	326.1	5.2482	5.8285
		PA6 30CF		
TCA	3.779	264.5	5.3407	6.7438
TCI	3.781	264.7	5.2874	7.1127
		D16T		
TCA	8.146	570.3	5.1964	-
TCI	8.152	570.6	5.2287	-

3.1.2. Experimental verification

doi:10.20944/preprints202312.0789.v1

The TCA and TCI brackets (30 samples in total) were cut using a milling machine from plates molded from a short-reinforced composite materials PA6 50GF, PA6 30CF and, for comparison with isotropic material, from an aluminum D16T plate. Mechanical tests of the brackets were carried out on MTS 322 machine (Figure 7). The results are presented in Figure 8 in terms of specific force and normalized deformation by the characteristic dimension (see Section 2.4). The normalized specific stiffness was calculated as the ratio of F/m to ◎/l in the elastic zone in all cases, where F is loading force, m is bracket mass, ◎◎is the displacement of the bracket lug along the line of force, l is the distance from the embedment to the axis of application of the force.

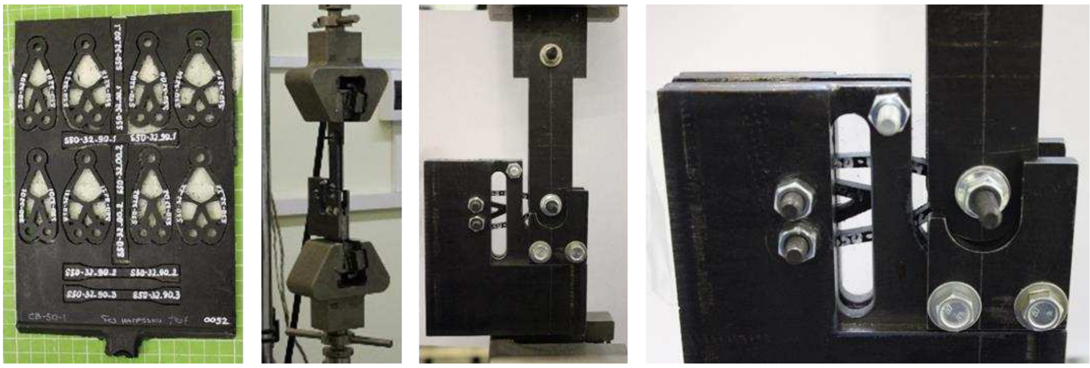

Figure 7. TCA and TCI brackets loading experiment.

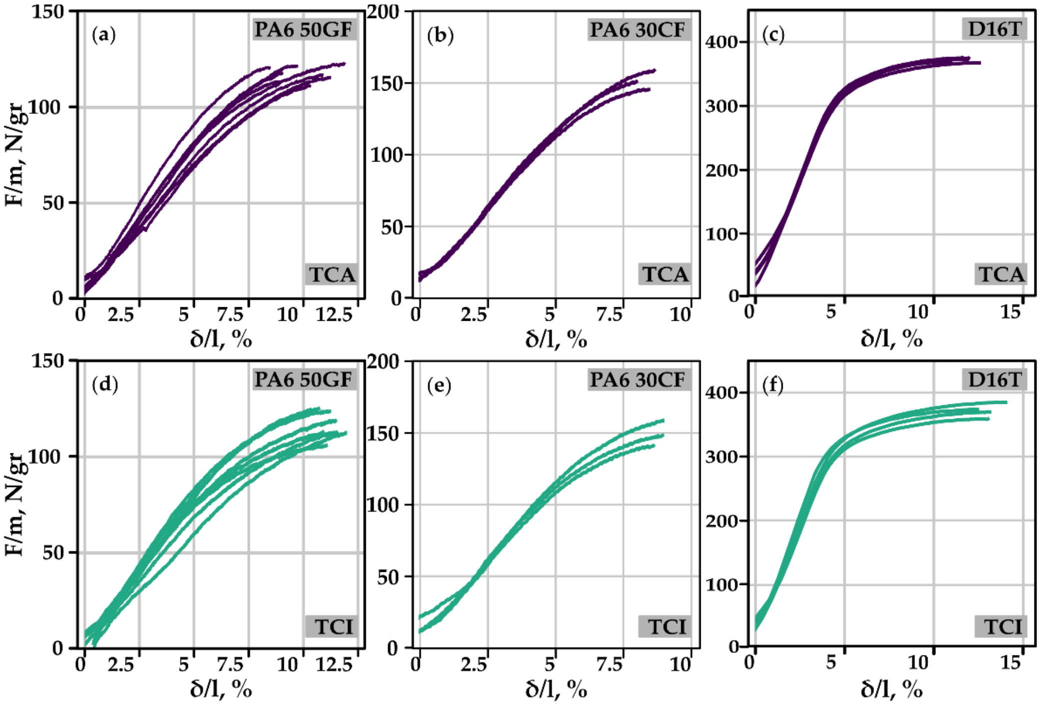

Figure 8. TCA and TCI experimental loading curves.

Non-linear structural analysis was performed on the obtained topologies to compare the numerical and experimental results (Figure 9). The experimental lines are summarized in the form of average values over the samples and the scatter field by the value of the standard deviation. The normalized specific stiffness of the numerical results was calculated from 25 to 50% of the maximal specific force for each TCA and TCI and material combination. For experimental results, it was calculated from 2.07 to 4.12% for PA6 50GF, from 4 to 5.74% for PA6 30CF, and from 1.5 to 3% for D16T. The integral characteristics of each structure as well as their normalized specific stiffness are presented in Table 3.

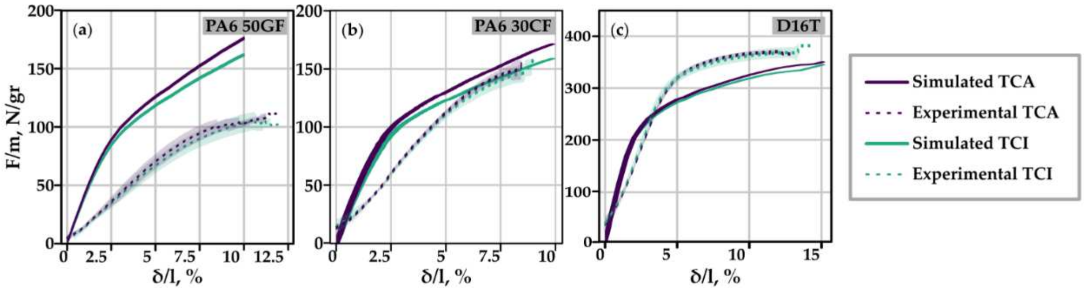

Figure 9. Specific force-normalized deformation curves of numerical and experimental TCA and TCI made of: (a) PA6 50GF; (b) PA6 30CF; (c) D16T.

Table 3. Normalized specific stiffness of TCA and TCI.

Topology	Normalized specific stiffness, N/gr		Percentage change from TCA to TCI, %
	TCA	TCI	
PA6 50GF	3883	3661	6.06
PA6 30CF	4621	4194	10.18
D16T	11474	11654	-1.54

The statistics of the experimentally obtained specific stiffness of TCA and TCI are shown in Table 4. The high coefficient of variation of D16T topologies results from the machining precision during manufacturing of these topologies.

Table 4. Statistics of normalized specific stiffness of TCA and TCI.

Material	Average, N/gr		Standard deviation, N/gr		Coefficient of variation, %		Percentage change from TCA to TCI, %
	TVA	TVI	TVA	TVI	TVA	TVI	
PA6 50GF	1551	1479	140	167	9.03	11.26	4.87
PA6 30CF	1833	1737	52	96	2.84	5.54	5.53
D16T	7192	7584	76	406	1.06	5.36	-5.17

3.2. Topology-optimal three-dimensional structures

3.2.1. Topology optimization and topology assessment

In Figure 10, the design region and boundary conditions for the TO are presented. The design region has dimensions of 105 x 60 x 10 mm. The optimization was carried out on a mesh of 163325 tetragonal elements, each with a size of 1.5 mm. The force F was applied to the center-right side element of the region, while the elements located at the left-side corners had a fixed displacement of 0 mm. The target volume fraction to be retained was set to 20%, and the minimum size of the structural elements was 6 mm. Anisotropic material, PA6 50 GF and PA6 30CF, as well as isotropic material D16T, were considered for the analysis.

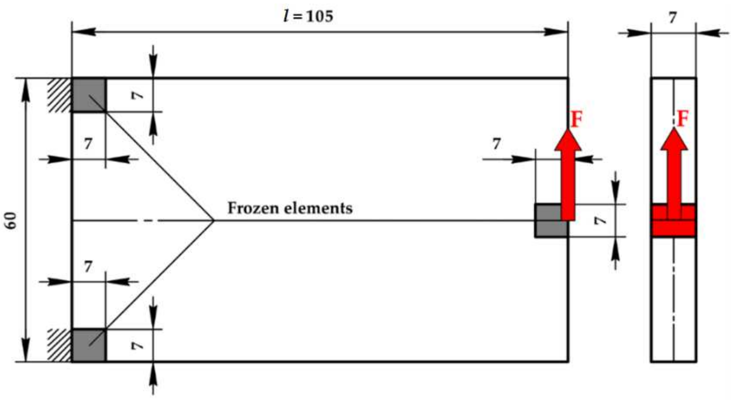

Figure 10. Topology optimization design region for the three-dimensional case.

As in the previous case of study, the resultant topology, considering anisotropy and isotropy, will be further referred to as TVA (Topology Variable Anisotropy) and TVI (Topology Variable case with Isotropy material), respectively. The convergence progress is illustrated in Figure 11, where a converged solution was achieved after 71 and 66 iterations, respectively. The resultant topologies are displayed in Figure 12. A comparison of the results in Figure 12 reveals that considering the material's anisotropy in topology optimization results in changes to the structural layout. In Figure 12b, the connections of the main structural members become more rounded, and some rods are added in the central area of the part.

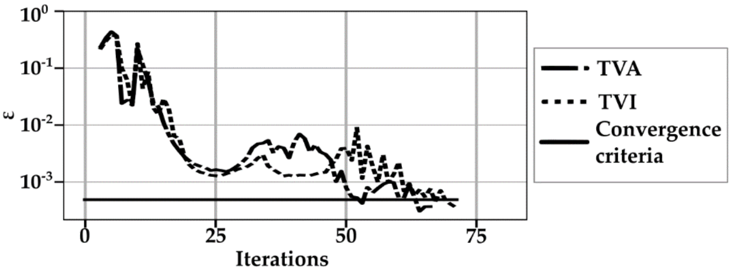

Figure 11. Topology optimization convergence plot by total strain energy relative error.

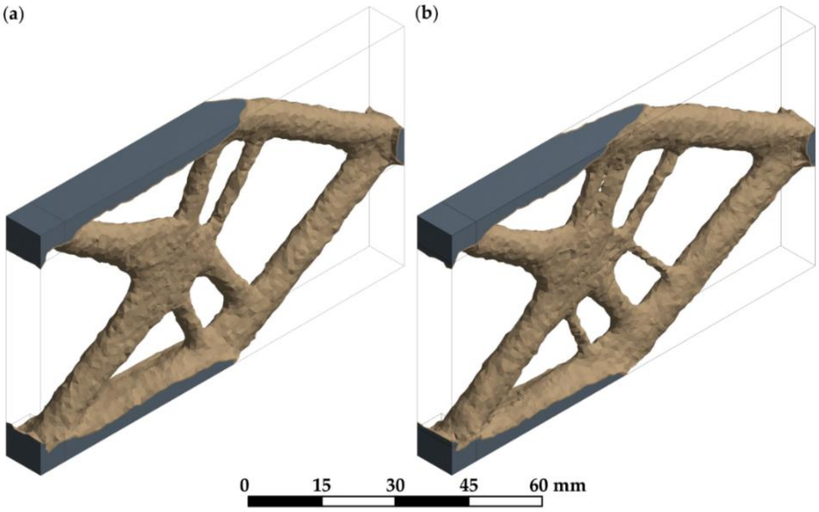

Figure 12. Obtained topologically optimal three-dimensional structures by using: (a) Fixed fiber orientation; (b) Variable fiber orientation.

3.1.2. Topology reconstruction

The resultant TO topologies from Section 3.2.1 are idealized results and are not final geometries ready for verification and manufacturing. They were manually reconstructed in Siemens NX. Figure 13 presents the baseline and reconstructed TVA and TVI topologies.

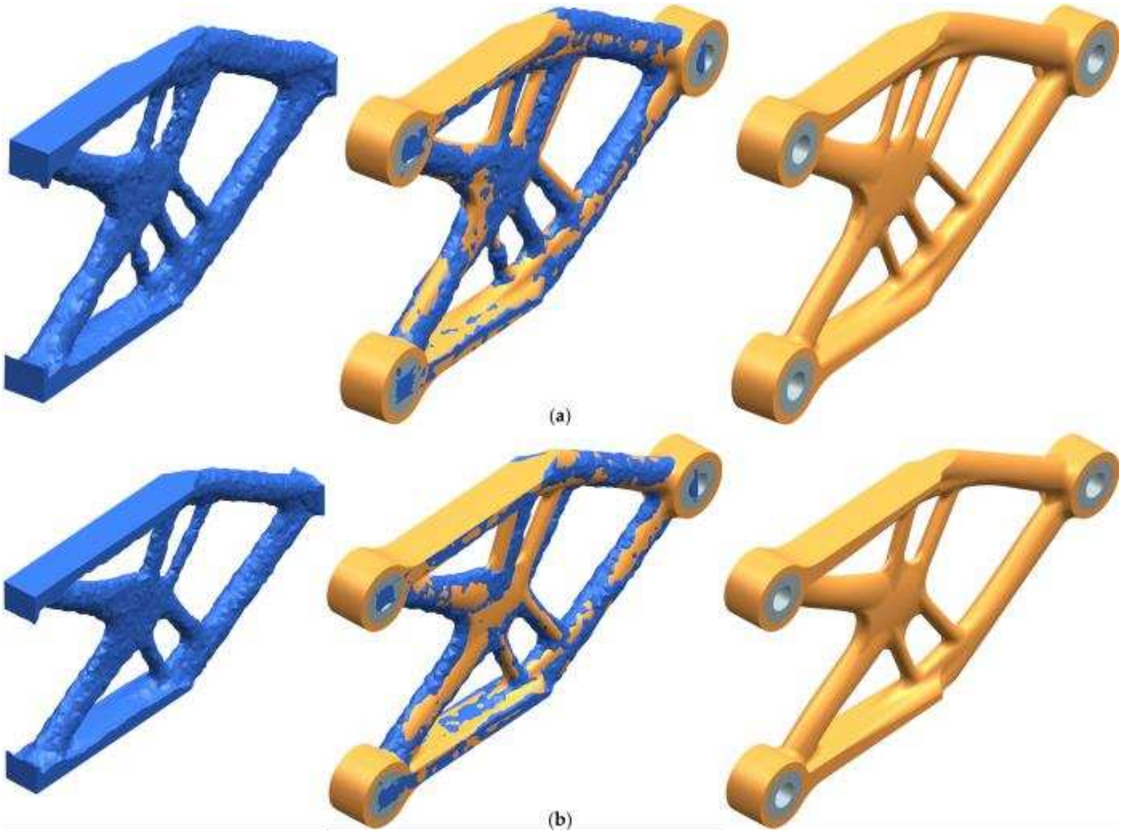

Figure 13. Topology reconstruction divided into three stages: Result of topology optimization (Baseline), baseline and reconstructed topology overlaying, and reconstructed geometry: (a) TVA; (b) TVI.

Verification was performed by comparing the fiber orientation tensor at three points within the topology and evaluating the LCF coefficient of the topologies in different reconstruction stages. Since injection molding simulation during TO was performed on a tetrahedral mesh, this mesh was evaluated as well. The internal-exported, baseline, and reconstructed topologies, where the fiber orientation tensor was extracted, and the components of their tensors are presented in Figure 14.

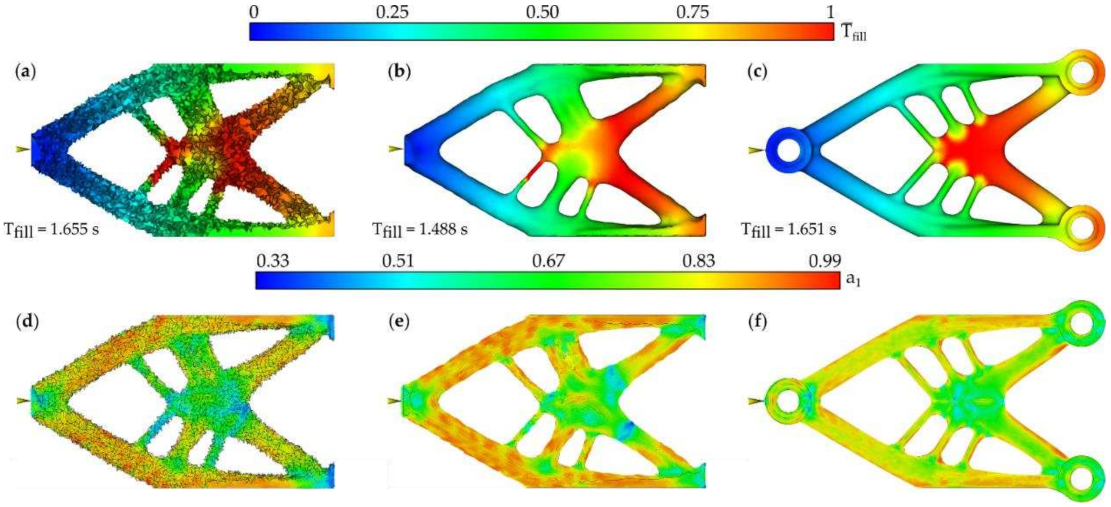

Figure 14. Flow field: (a) Internal-exported TVA; (b) Baseline TVA; (c) Reconstructed TVA; (b) Reconstructed TVI. Fiber orientation tensor: (d) Internal-exported TVA; (e) Baseline TVA; (f) Reconstructed TVA.

The internal-exported, baseline, and reconstructed topologies were subject to lineal structural analysis using linear PA6 50GF, PA6 30CF and D16T. Figure 15 illustrates the von Mises-based and

Tsai-Hill failure criteria fields for the baseline, smoothed TVA and reconstructed TVA and TVI when the topologies were subjected to loads corresponding to $^F/_M$ = 70 N/gr. Table 5 displays the corresponding C_K values of both topologies and provides a comparison between them.

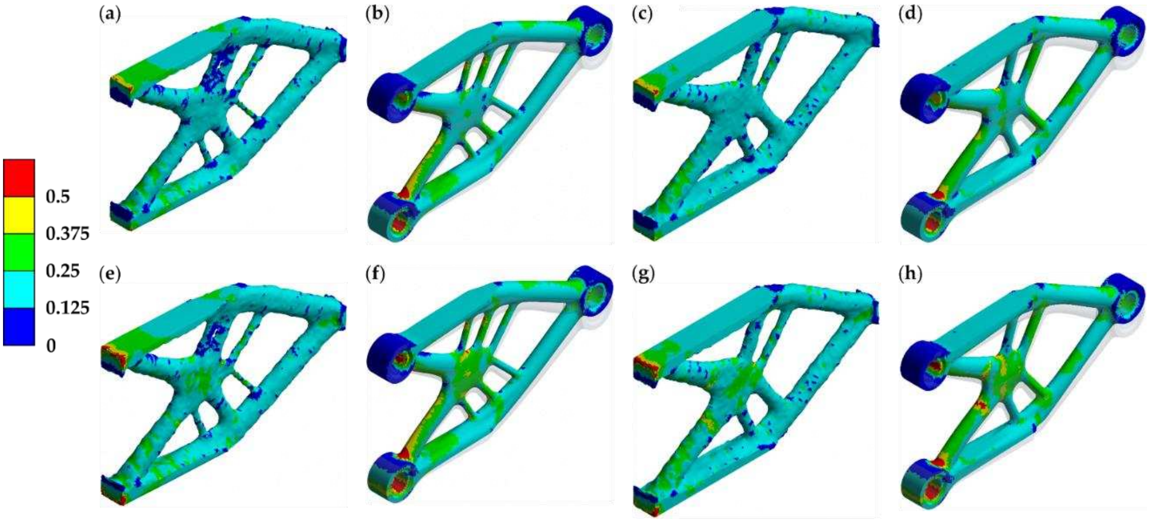

Figure 15. Tsai-Hill failure criterion field: (a) Baseline TVA; (b) Reconstructed TVA; (c) Baseline TVI; (d) Reconstructed TVI. Equivalent stress (von Mises-based) failure criterion field: (e) Baseline TVA; (f) Reconstructed TVA; (g) Baseline TVI; (h) Reconstructed TVI.

The failure criteria F and volume dV of each element, as described in equations (3) and (7), were multiplied and summed to calculate the LCF coefficient. The LCF coefficient of each topology and material combination is presented in Table 5. The characteristic linear dimension l for the baseline topologies is 105 mm, whereas for the reconstructed topologies, it is 102.55 mm. The ultimate tensile stress σ^{UTS} for PA6 30CF topologies is 169.35 MPa, while for D16T topologies, it is 476 MPa. The percentage change is calculated with respect to the correspondent baseline topology.

Table 5. LCF coefficient of internal-exported, baseline, and reconstructed TVA and TVI.

Topology	**Baseline**				**Reconstructed**				**Percentage difference from baseline to reconstructed**	
	m, g	**f, N**	**C_K^{eq}**	**C_K^{TH}**	**m, g**	**f, N**	**C_K^{eq}**	**C_K^{TH}**	**C_K^{eq}**	**C_K^{TH}**
PA6 50GF										
TVA	22.94	1606	3.3183	3.4341	25.59	1791	3.5230	3.6541	5.98%	6.21%
TVI	23.24	1627	3.3214	3.4437	26.17	1832	3.5481	3.6926	6.60%	6.98%
PA6 30CF										
TVA	18.62	1304	3.3225	3.6881	20.76	1448	3.5273	3.9025	5.98%	5.65%
TVI	18.86	1320	3.3238	3.7103	21.24	1481	3.5539	3.9799	6.69%	7.01%
D16T										
TVA	40.15	2810	3.3122	-	47.34	3314	3.5707	-	7.51%	-
TVI	40.66	2846	3.3176	-	48.36	3386	3.5892	-	7.86%	-

3.2.3. Experimental validation

TVA and TVI brackets are made by injection molding (Figure 16). To strengthen the lugs, aluminium embedded elements (bushings) were added. The simulation of the injection molding process was qualitatively validated by comparing the real and simulated flow at a specific filling time (Figure 17). The used at design stage flow model makes it possible to predict the material distribution during the molding process with good accuracy.

Figure 16. TVA and TVI brackets manufacturing process on an injection molding machine.

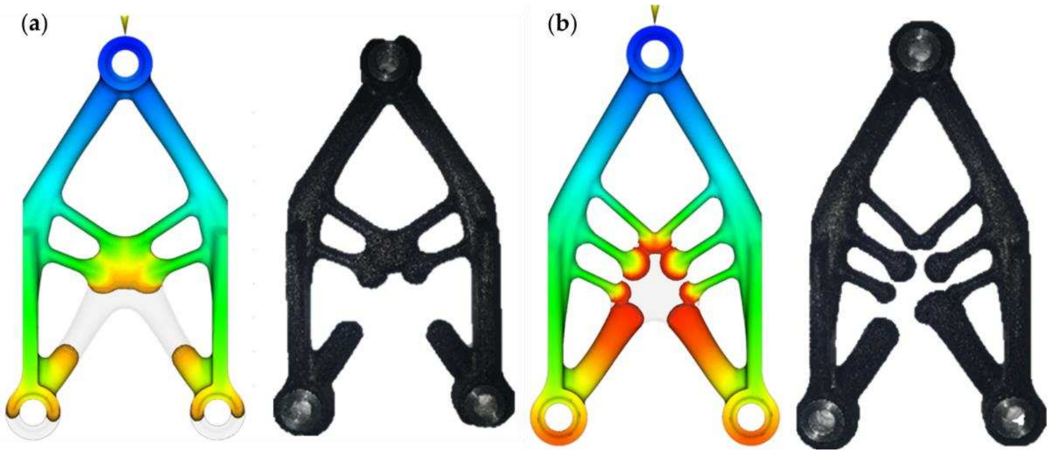

Figure 17. Flow field: (**a**) Simulated and experimental flow of TVA; (**b**) Simulated and experimental flow of TVI.

Fiber orientation was assessed by comparing the numerical fiber orientation against the real fiber orientation, which was observed under an electronic microscope, Tescan Vega 3T, at the fracture zone. Figure 18 shows the points at which the fiber orientation was evaluated.

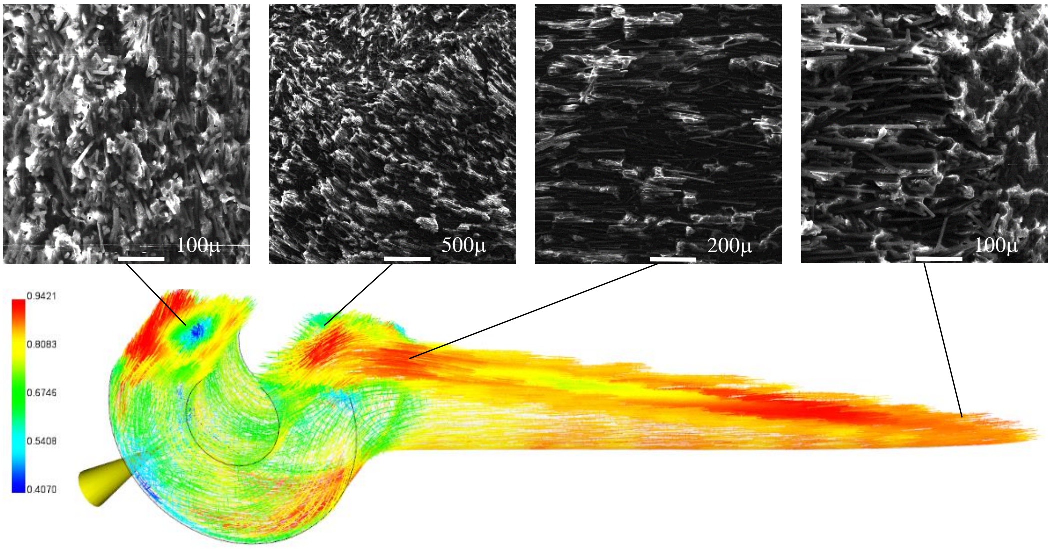

Figure 18. The fiber orientation at different fracture zones.

Mechanical tests of the TVA and TVI brackets from PA6 50GF, PA6 30CF and D16T (51 samples in total) were carried out on MTS 322 machine (Figure 19). The experimentally obtained specific force-normalized deformation curves for TVA and TVI brackets are presented in Figure 20.

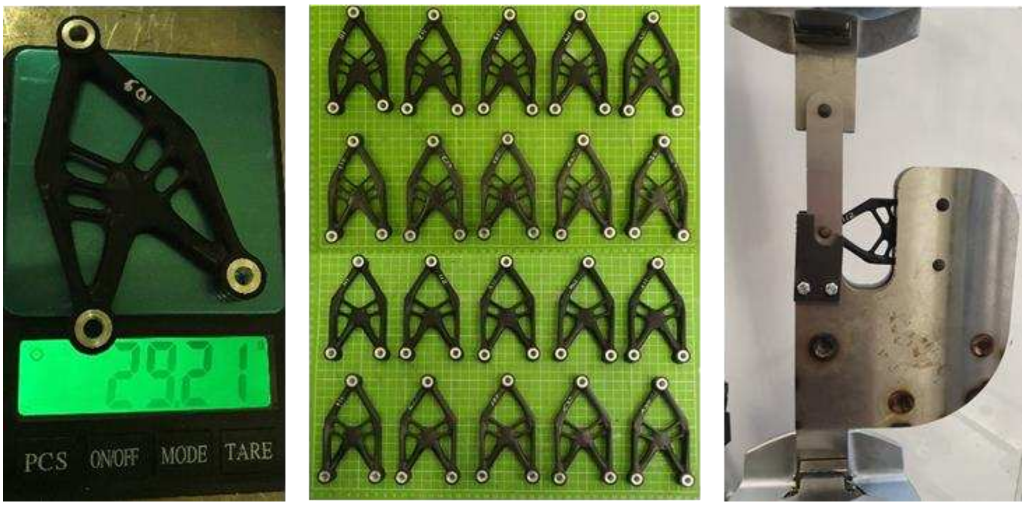

Figure 19. TVA and TVI brackets testing.

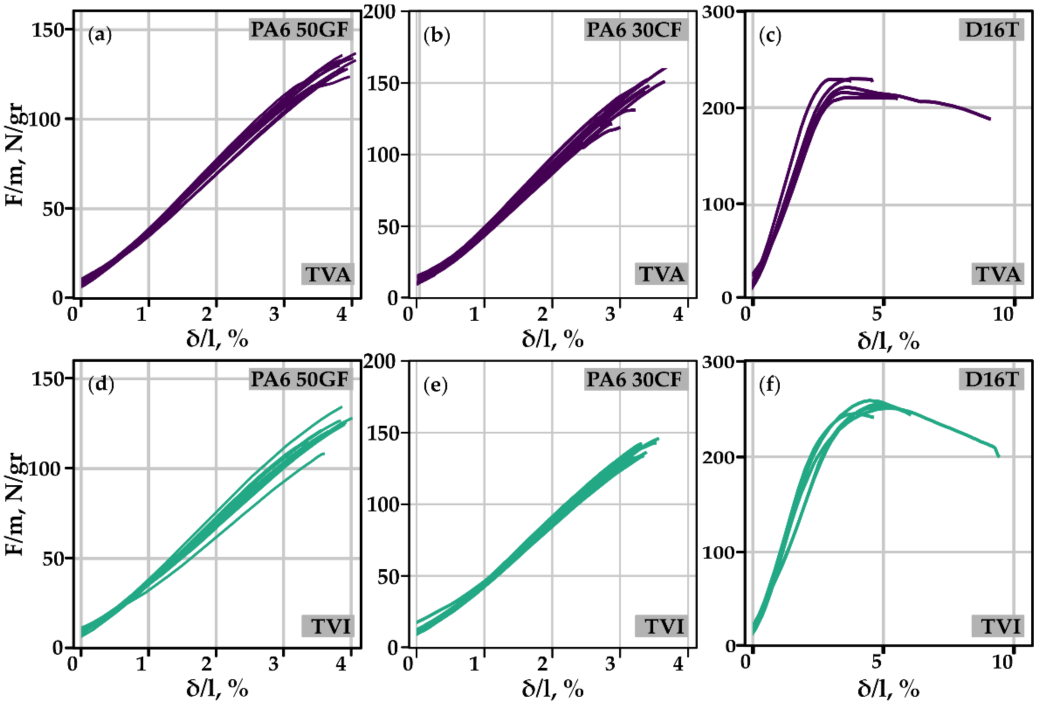

Figure 20. TVA and TVI made from PA6 50GF, PA6 30CF, D16T bracket loading experiment.

Non-linear structural analysis of TVA and TVI brackets was performed on the reconstructed topologies to compare the numerical and experimental results (Figure 21). The experimental lines are summarized in the form of average values over the samples and the scatter field by the value of the standard deviation.

The normalized specific stiffness was calculated in the elastic zone in all cases with respect to normalized deformation. For the numerical results, the normalized specific stiffness ranged from 5.66 to 13.17%, while for the experimental results, it ranged from 7.5 to 15.8% for PA6 50GF and from 8.5 to 17.3% for PA5 30CF and D16T. The integral characteristics of each structure, as well as their normalized specific stiffness, are presented in Table 6.

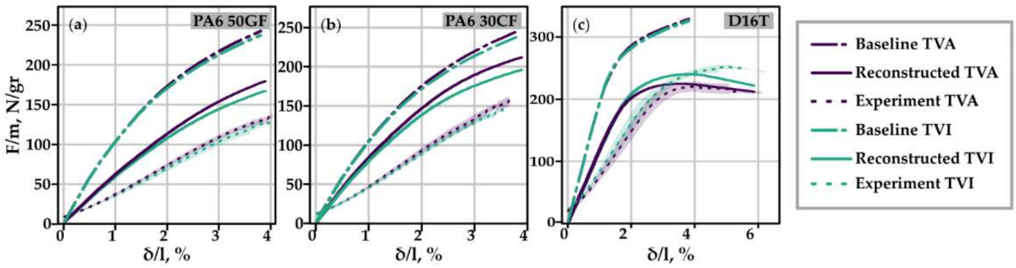

Figure 21. Specific force-normalized deformation curves of numerical and experimental TVA and TVI made of: (a) PA6 50GF; (b) PA6 30CF; (c) D16T.

Table 6. Normalized specific stiffness and mass characteristics of the baseline and reconstructed TVA and TVI.

Material	Topology	Normalized specific stiffness, N/gr		Percentage change from TVA to TVI, %
		TVA	TVI	
PA6 50GF	Baseline	7250	7187	0.88
	Reconstructed	5500	5260	4.56
PA6 30CF	Baseline	8993	8924	0.77
	Reconstructed	7209	6893	4.58
D16T	Baseline	19737	19869	-0.66
	Reconstructed	11838	11613	1.92

The statistics of the experimentally obtained specific stiffness for TVA and TVI are shown in Table 7. The high coefficient of variation of D16T topologies is attributed to the machining precision during the manufacturing of these topologies.

Table 7. Statistics of the normalized specific stiffness of reconstructed TVA and TVI.

Material	Average, N/gr		Standard deviation, N/ gr		Coefficient of variation, %		Percentage change from TVA to TVI, %
	TVA	TVI	TVA	TVI	TVA	TVI	
PA6 50GF	3529	3289	179	267	5.09	8.13	7.30
PA6 30CF	4533	4290	216	187	4.77	4.36	5.66
D16T	7293	7875	775	1150	10.63	14.60	-7.39

4. Discussion

Assessment of the topologies by the LCF coefficient (see Sections 3.1.1 and 3.1.2) reveals that the classic coefficient C_K is more suitable for structures made of isotropic materials. The classic C_K does not convey any information regarding the anisotropy, making it incapable of accurately estimating the quality of structures made from anisotropic material. For example, the classic C_K indicates the advantage of TCI made from anisotropic materials over TCA, despite the latter having lower specific stiffness (see Tables 2 and 3). The C_K^{TH} incorporates the effect of anisotropy on the stress-state of the structure by optimizing the placement of structural elements to achieve more efficient mold filling. The minimal C_K^{TH} values of the TCA and TCI correspond to the maximal specific stiffness of these topologies. However, a significant drawback arises from the fact that the integral over the volume of the failure criteria is the product of the average criteria values over the volume, making LCF insensitive to both under and over-stressed elements. We recommend evaluating the structure's topology not only using any of the possible formulations of the LCF coefficient but also employing a metric based on the coefficient of variance of the failure criteria (where the average and deviation are calculated from the failure criteria value over the volume). Moreover, reformulating the objective function to minimize both the average and deviation of the total strain energy of the topology should lead to a more equally strong structure.

The results obtained in Section 3 confirm that considering anisotropy during TO increases the normalized specific stiffness of the resultant topologies. Specifically, the normalized specific stiffness increased numerically by 6.06–10.18% and 0.77–0.88% in the two- and three-dimensional cases of study, respectively (see Sections 3.1.2 and 3.2.3). The impact of considering anisotropy during TO is more pronounced in the 2D case. It can be assumed that the contrast in the normalized specific stiffness between the two- and three-dimensional cases is due to the regular orientation of the flow—and the fibers within it—along the structural elements in the three-dimensional case, causing the mechanical characteristics in these elements to be closer to those of the 0° oriented material. The increase in the change in the normalized specific stiffness of the reconstructed topologies compared to the baseline topologies (see Section 3.2.3) can be attributed to inaccuracies introduced by the CAD engineer during reconstruction and the replacement of fixed supports with bolted joints. Moreover, an increment is observed when comparing the C_K^{TH} of the baseline and reconstructed topologies, suggesting that C_K^{TH} and the normalized specific stiffness are correlated and that C_K^{TH} serves as an indicator of the degree of pristine (flawless) structure compared to the baseline topology. The experimental results showed that the normalized specific stiffness increased by 4.84–5.63% and 5.66–7.30% in the two- and three-dimensional cases, respectively (see Sections 3.1.2 and 3.2.3). This indicates that two important points in this work: making the stiffness matrix dependent on the fiber orientation tensor, and obtaining the fiber orientation tensor by solving the Navier-Stokes equations along with the Folgar-Tucker's continuity equation allow us to achieve a stiffer structure (since the 2D case does not account for these points). The deviation of the numerical from the experimental results can be attributed to differences in the loading scheme, the material model, and the omission of the weld lines during the numerical calculation. During the experiment with TVA and TVI brackets, it was noted that the poor adhesion between the aluminum bushing and the SFRP structure generated a weak joint interfacial strength, which could be the reason for the lower normalized specific stiffness than that predicted by the numerical model. Therefore, the investigation of the adhesion of aluminum and titanium alloys with SFRP can be part of future studies.

Regarding the topology, it is evident that TO attempts to orient the structural elements along the fiber direction when accounting for anisotropy, in contrast to TO in an isotropic medium, where the elements are positioned further from the symmetry line to reduce bending moments. The same topology distribution can be observed in the results of the work [63], where fiber orientation was simultaneously and sequentially considered. Therefore, is confirmed that for better structural performance of the structural elements, they should be oriented in the direction of the fiber, in other words, in the direction of maximum stiffness. Moreover, this last statement also demonstrates the minimal difference between the topologies in the three-dimensional case.

We have several recommendations for improving the repeatability of this work. First, the maximum strain rate at which the topologies are loaded during the tensile test should be 0.01 s^{-1}. Second, the effect of boundary conditions should be minimized to achieve higher contrast between solutions, alternatively, different boundary conditions should be investigated. For instance, increasing the design region, placing the loads further from the support, or analyzing complex loading schemes such as the geometry presented in the work [82]. Third, changing the type of material model used during TO from linear to non-linear should be considered, as previous works [83] have demonstrated that this leads to stronger structures. Finally, solving for the fiber orientation tensor during TO should be performed on a smooth surface (see Figure 14).

5. Conclusion

In this work, a methodology for obtaining topology-optimal structures made of short fiber-reinforced composites (SFRC) while considering the material's anisotropy was presented. The calculation of the composite material's stiffness matrix was performed using the fiber orientation tensor, which was obtained by solving the plastic molding equations for non-Newtonian fluids. Both calculations and experimental results confirmed that accounting for the material's anisotropy can significantly enhance the rigidity of structures made from short-reinforced composite materials.

In instances where predetermined anisotropy was taken into consideration, the orientation of the reinforcing fibers led to stiffness increases ranging from 5 to 10%. In the case of molding truss-type structures, the stiffness increase was somewhat lower, ranging from 0.8 to 7.3%. This discrepancy arises from the fact that, in truss-type structures, the majority of the fibers align with the load-bearing elements of the truss, while the truss contributes less to the overall rigidity of the structure.

Furthermore, the results obtained using this technique were compared with those of topology-optimal structures. Thus, the increase in stiffness is also expressed as a percentage. In specific applications, especially within the aerospace industry, such an increase in stiffness can prove to be significantly advantageous.

This work demonstrates that the modified C_K^{TH}, in terms of the Tsai-Hill failure criterion, can be effectively employed in the design of fiber-reinforced polymer-based composite structures. It's worth noting that the C_K approach can be formulated using other failure criteria as well. For instance, the Tsai–Wu failure criterion may be more appropriate when distinguishing between tension and compression strengths is crucial.

Currently, various options exist for assessing weight efficiency using dimensionless criteria. Nevertheless, this field has yet to achieve a comprehensive form, and the approach proposed in this work contributes to the advancement of dimensionless methods for assessing the quality of structures made from short-reinforced composite materials.

Author Contributions: Conceptualization, E.Ku.; methodology, E.Ku.; validation, E.Ku. and O.U.E.B.; software, E.Ku. and E.Ki.; formal analysis, O.U.E.B. and E.Ku.; investigation E.Ku., O.L., E.Ki. and O.U.E.B.; data curation, O.U.E.B., E.Ku.; writing—original draft preparation, O.U.E.B. and E.Ku.; writing—review and editing, O.U.E.B., E.Ki., O.L. and E.Ku.; visualization, O.U.E.B. and O.L.; supervision, E.Ku.; project administration, E.Ku.; funding acquisition, E.Ku. All authors have read and agreed to the published version of the manuscript.

Funding: The research on the design quality of short-reinforced composite-material structures was funded by the Russian Science Foundation, grant number 22-79-10309.

Data Availability Statement: The data presented in this study are available on request from the corresponding author.

Acknowledgments: We would like to express our special thanks of gratitude to Valery Komarov for advancing the use of dimensionless numbers in structural design and structural engineering theory. We would like to express our gratitude to Igor Slovtsov and Valery Komarov for bringing to our attention the potential usage of SFRC in aerospace structures. We would also like to extend our gratitude to Aleksandr Pavlov and Stanislav Selivanov for their support in performing the tensile test, and to Pladep Ltd. for their support during injection molding.

Conflicts of Interest: The authors declare no conflict of interest. The funders had no role in the design of the study; in the collection, analyses, or interpretation of data; in the writing of the manuscript, or in the decision to publish the results.

References

1. Zhitomirskiy, G. Konstruktsiya Samoletov: Uchebnoye Posobiye [Aircraft Structure: Textbook]; 4th ed.; Mashinostroyeniye: Moscow, 2018; ISBN 978-5-9500364-8-4.
2. Yendogur, A. Proyektirovaniye Aviatsionnykh Konstruktsiy: Proyektirovaniye Konstruktsiy Detaley i Uzlov [Aircraft Structural Design: Structural Design of Parts and Assemblies]; MAI-Print: Moscow, 2009; ISBN 9785703521038.
3. Kobelev, V. Design and Analysis of Composite Structures for Automotive Applications : Chassis and Drivetrain; ISBN 9781119513841.
4. Spacecraft Structures; Springer Berlin Heidelberg: Berlin, Heidelberg, 2008; ISBN 978-3-540-75552-4.
5. Alejandro Ortiz Morales, F.; Bejarano, W.; Zorto, F.; Mejuto, J.; Ortiz, F.; Bejarano Diana Rosales, W. Chassis Optimization of a 1U Cubesat Made in a Developing Country Estudio Arqueoastronómico Del Parque Arqueológico de El Puente View Project Participación Científica En La Misión a Marte MEIGA-METNET-PRECURSOR View Project Chassis Optimization of a 1U Cubesat Made in a Developing Country;
6. Feng, Y.; Wu, X.; Chen, W.; Xie, Y.; Yu, T.; Hao, Y. Optimal Design of Space Assembly Microsatellite Structure Based on Sequential Quadratic Programming. Aircraft Engineering and Aerospace Technology 2022, doi:10.1108/AEAT-02-2021-0057.
7. Watanabe2009.
8. Kawachi, T.; Kimoto, N.; Tsunemi, Y. Stiffness Increase and Weight Reduction Based on Stiffness Evaluation Techniques;
9. Formula_1_-_technical_regulations_-_2022_-_iss_9_-_2022-02-18.
10. Huh, J.; Kwon, S. A Practical Design Approach for a Single-Stage Sounding Rocket to Reach a Target Altitude. Aeronautical Journal 2022, 126, 1084–1100, doi:10.1017/aer.2022.18.
11. Gudmundsson, S. Aircraft Cost Analysis. In General Aviation Aircraft Design; Elsevier, 2014; pp. 33–53.

12. Vasigh Bijan and Azadian, F. Aircraft Financial and Operational Efficiencies. In Aircraft Valuation in Volatile Market Conditions: Guiding Toward Profitability and Prosperity; Springer International Publishing: Cham, 2022; pp. 113–163 ISBN 978-3-030-82450-1.
13. Shukla, S.; Singh, H.V.; Mishra, L. Improvement In Design Of Engines To Reduce Emissions In Aircarft And Increase Fuel Efficiency. In Outcomes Of Best Practices In Classroom Research; L Ordine Nuovo Publication: New Delhi, 2021 ISBN 978-93-92995-10-1.
14. Peters, M.; Kumpfert, J.; Ward, C.H.; Leyens, C. Titanium Alloys for Aerospace Applications. Adv Eng Mater 2003, 5, 419–427.
15. Tseng, H.-C.; Chang, R.-Y.; Hsu, C.-H. Numerical Investigations of Fiber Orientation Models for Injection Molded Long Fiber Composites;
16. Advanced Aerospace Materials; Buhl, H., Ed.; Springer Berlin Heidelberg: Berlin, Heidelberg, 1992; ISBN 978-3-642-50161-6.
17. Garvey, R.E.; Andriulli, J.B.; Mckeever, J.W. Minimum-Gage, Maximum-Stiffness Graphite/ Thermoplastic Spacecraft Structures;
18. Maleki, H.; Durães, L.; Portugal, A. An Overview on Silica Aerogels Synthesis and Different Mechanical Reinforcing Strategies. J Non Cryst Solids 2014, 385, 55–74, doi:10.1016/j.jnoncrysol.2013.10.017.
19. Tiwary, A.; Kumar, R.; Chohan, J.S. A Review on Characteristics of Composite and Advanced Materials Used for Aerospace Applications. In Proceedings of the Materials Today: Proceedings; Elsevier Ltd, 2021; Vol. 51, pp. 865–870.
20. Tang, S.; Hu, C. Design, Preparation and Properties of Carbon Fiber Reinforced Ultra-High Temperature Ceramic Composites for Aerospace Applications: A Review. J Mater Sci Technol 2017, 33, 117–130, doi:10.1016/j.jmst.2016.08.004.
21. Mangalgiri, P.D. Composite Materials for Aerospace Applications; 1999; Vol. 22;.
22. Bhat, A.; Budholiya, S.; Raj, S.A.; Sultan, M.T.H.; Hui, D.; Shah, A.U.M.; Safri, S.N.A. Review on Nanocomposites Based on Aerospace Applications. Nanotechnol Rev 2021, 10, 237–253, doi:10.1515/ntrev-2021-0018.
23. Romero-Fierro, D.; Bustamante-Torres, M.; Bravo-Plascencia, F.; Esquivel-Lozano, A.; Ruiz, J.-C.; Bucio, E. Recent Trends in Magnetic Polymer Nanocomposites for Aerospace Applications: A Review. Polymers (Basel) 2022, 14, 4084, doi:10.3390/polym14194084.
24. Rajput, A.; Upma; Shukla, S.K.; Thakur, N.; Debnath, A.; Mangla, B. Advanced Polymeric Materials for Aerospace Applications. In Aerospace Polymeric Materials; Wiley, 2022; pp. 117–136.
25. Sokolowski, W.M.; Tan, S.C. Advanced Self-Deployable Structures for Space Applications. J Spacecr Rockets 2007, 44, 750–754, doi:10.2514/1.22854.
26. Liu, Y.; Du, H.; Liu, L.; Leng, J. Shape Memory Polymers and Their Composites in Aerospace Applications: A Review. Smart Mater Struct 2014, 23, doi:10.1088/0964-1726/23/2/023001.
27. Soutis, C. Fibre Reinforced Composites in Aircraft Construction. Progress in Aerospace Sciences 2005, 41, 143–151.
28. García, J.A. Study On 3d Printing With Fiber Reinforcement And Its Aerospace Applications;
29. Öztoprak, N. Novel AA7075/AA2124-SiC-17p Laminated Structures for Aerospace Applications: A Comparative Study into the Mechanical Performance of PA6 and PA66 Composite Interlayers. Journal of Composite Materials 2022, 0, doi:10.1177/00219983221135050.
30. Neveu, F.; Cornu, C.; Olivier, P.; Castanié, B. Manufacturing and Impact Behaviour of Aeronautic Overmolded Grid-Stiffened Thermoplastic Carbon Plates. Compos Struct 2022, 284, doi:10.1016/j.compstruct.2022.115228.
31. Arevo Applications Available online: https://arevo.com/applications?lang=en (accessed on 9 November 2022).
32. Aircraft Seat Support | Anisoprint Available online: https://anisoprint.com/cases/aircraft-seat-support/ (accessed on 9 November 2022).
33. Composite Tool for Turbine Blade Production | Anisoprint Available online: https://anisoprint.com/cases/composite-tool-for-wind-blade-production/ (accessed on 9 November 2022).
34. D2-Concepts.
35. Kassapoglou, C. Design and Analysis of Composite Structures; Wiley, 2013; ISBN 9781118401606.
36. Lake, M.S. NASA Technical Paper 3210 Stiffness and Strength Tailoring in Uniform Space-Filling Truss Structures; 1992;
37. Campo, G.A.; Vettorello, A.; Giacalone, M. Optimization Methodology for Continuous Heterogeneous Structures: A Preliminary Design of an Engine Mounting Bracket. In Proceedings of the Key Engineering Materials; Trans Tech Publications Ltd, 2020; Vol. 827 KEM, pp. 116–121.
38. Vasiliev, V. v.; Barynin, V.A.; Razin, A.F. Anisogrid Composite Lattice Structures - Development and Aerospace Applications. Compos Struct 2012, 94, 1117–1127, doi:10.1016/j.compstruct.2011.10.023.

39. Ermolaeva, N.S.; Castro, M.B.G.; Kandachar, P. v. Materials Selection for an Automotive Structure by Integrating Structural Optimization with Environmental Impact Assessment. Mater Des 2004, 25, 689–698, doi:10.1016/j.matdes.2004.02.021.
40. Sienz, J.; Luege, M.; Fuerle, F. Continuous Optimization in Aerospace Structures. In Encyclopedia of Aerospace Engineering; John Wiley & Sons, Ltd, 2010.
41. Pettit, C.L.; Grandhi, R. v Multidisciplinary Optimization of Aerospace Structures with High Reliability; 2000;
42. Komarov, V.A.; Kishov, E.A.; Kurkin, E.I.; Charkviani, R. v. Aircraft Composite Spoiler Fitting Design Using the Variable Density Model. In Proceedings of the Procedia Computer Science; Elsevier, 2015; Vol. 65, pp. 99–106.
43. Komarov, V.; Kurkin, E.; Spirina, M.; Kishov, E. Estimation of Weight Efficiency of Topologically Optimal Aerospace Structures. In Proceedings of the Proceedings of 9th International Conference on Recent Advances in Space Technologies, RAST 2019; Institute of Electrical and Electronics Engineers Inc., June 1 2019; pp. 95–101.
44. Rahmani, M.; Behdinan, K. Design Optimization of Multifunctional Aerospace Structures. In Advanced Multifunctional Lightweight Aerostructures; Design, Development, and Implementation; Wiley, 2021; pp. 93–108.
45. Zhu, J.H.; Zhang, W.H.; Xia, L. Topology Optimization in Aircraft and Aerospace Structures Design. Archives of Computational Methods in Engineering 2016, 23, 595–622, doi:10.1007/s11831-015-9151-2.
46. Li, B.; Liu, H.; Zheng, S. Multidisciplinary Topology Optimization for Reduction of Sloshing in Aircraft Fuel Tanks Based on SPH Simulation. Structural and Multidisciplinary Optimization 2018, 58, 1719–1736, doi:10.1007/s00158-018-1995-2.
47. Maute, K.; Reich, G.W. Integrated Multidisciplinary Topology Optimization Approach to Adaptive Wing Design. J Aircr 2006, 43, 253–263, doi:10.2514/1.12802.
48. Komarov, A. Osnovy Proyektirovaniya Silovykh Konstruktsiy [Fundamentals of Load-Carrying Structure Design]; Kuybyshev book publ.: Kuybyshev, 1965;
49. Komarov, V. Ratsional'noye Proyektirovaniye Silovykh Aviatsionnykh Konstruktsiy [Rational Design of Load-Carrying Aircraft Structures]. D. in Technical Sciences thesis, Kuibyshev Aviation Institute: Kuibyshev, 1974.
50. Komarov, V. Proyektirovaniye Silovykh Skhem Aviatsionnykh Konstruktsiy [Design of Load-Carrying Diagrams of Aircraft Structures]. In Aktual'nyye problemy aviatsionnoy nauki i tekhniki [Actual Problems of Aviation Science and Technology]; Lavrentyev, M., Ed.; Mashinostroyeniye: Moscow, 1984; p. 278.
51. Komarov, V. Design of Aircraft Structures on the Basis of Discrete Models. In Optimal Design: Theory and Applications to Materials and Structures; Vasiliev, V., Gurdal, Z., Eds.; Technomic Publishing Company: Lancaster, Pennsylvania, 1999; p. 330 ISBN 9781566766869.
52. Bendsøe, M.P.; Kikuchi, N. Generating Optimal Topologies in Structural Design Using a Homogenization Method. Comput Methods Appl Mech Eng 1988, 71, 197–224.
53. Bendsøe, M.P. Optimization of Structural Topology, Shape, and Material; Springer Berlin Heidelberg: Berlin, Heidelberg, 1995; ISBN 978-3-662-03117-9.
54. de Luca, A.; Caputo, F. A Review on Analytical Failure Criteria for Composite Materials. AIMS Mater Sci 2017, 4, 1165–1185, doi:10.3934/matersci.2017.5.1165.
55. Paris, F.; Washington, G. A Study of Failure Criteria of Fibrous Composite Materials; 2001;
56. HD-R138 091 A Survey Of Macroscopic Failure Criteria For Composite;
57. Komarov, V.A.; Weisshaar, T.A. New Approach to Improving the Aircraft Structural Design Process. J Aircr 2002, 39, 227–233, doi:10.2514/2.2943.
58. Komarov, V.A. Dimensionless Criterion of Power Perfection of a Structure. Mechanics of Solids 2018, 53, 385–396, doi:10.3103/S0025654418040040.
59. Komarov, V.A. Design and material. Ontology of designing 2023, 13(2), 175–191, doi: 10.18287/2223-9537-2023-13-2-175-191.
60. Nomura, T.; Kawamoto, A.; Kondoh, T.; Dede, E.M.; Lee, J.; Song, Y.; Kikuchi, N. Inverse Design of Structure and Fiber Orientation by Means of Topology Optimization with Tensor Field Variables. Compos B Eng 2019, 176, doi:10.1016/j.compositesb.2019.107187.
61. Papapetrou, V.S.; Patel, C.; Tamijani, A.Y. Stiffness-Based Optimization Framework for the Topology and Fiber Paths of Continuous Fiber Composites. Compos B Eng 2020, 183, doi:10.1016/j.compositesb.2019.107681.
62. Hu, Z. A Review on the Topology Optimization of the Fiber-Reinforced Composite Structures. Aerospace technic and technology 2021, 54–72, doi:10.32620/aktt.2021.3.07.
63. Caivano, R.; Tridello, A.; Paolino, D.; Chiandussi, G. Topology and Fibre Orientation Simultaneous Optimisation: A Design Methodology for Fibre-Reinforced Composite Components. Proceedings of the Institution of Mechanical Engineers, Part L: Journal of Materials: Design and Applications 2020, 234, 1267–1279, doi:10.1177/1464420720934142.

64. Silva, A.L.F. da; Salas, R.A.; Nelli Silva, E.C.; Reddy, J.N. Topology Optimization of Fibers Orientation in Hyperelastic Composite Material. Compos Struct 2020, 231, doi:10.1016/j.compstruct.2019.111488.
65. Park, S.W.; Choi, J.H.; Lee, B.C. Multi-Objective Optimization of an Automotive Body Component with Fiber-Reinforced Composites. Structural and Multidisciplinary Optimization 2018, 58, 2203–2217, doi:10.1007/s00158-018-2008-1.
66. Ospald, F.; Herzog, R. SIMP Based Topology Optimization for Injection Molding of SFRPs. In Proceedings of the SIMP based Topology Optimization for Injection Molding of SFRPs; Braunschweig, June 2017; p. 8.
67. Folgar, F.; Tucker III, C.L. Orientation Behavior of Fibers in Concentrated Suspensions. Journal of Reinforced Plastics and Composites 1984, 3, 98–119.
68. Advani, S.G.; Tucker, C.L. The Use of Tensors to Describe and Predict Fiber Orientation in Short Fiber Composites. J Rheol (N Y N Y) 1987, 31, 751–784, doi:10.1122/1.549945.
69. Kurkin, E.; Kishov, E. Programma AnisoTopo Postroyeniya Anizotropnykh Matrits Zhestkosti Elementov v Zadachakh Topologicheskoy Optimizatsii Konstruktsiy Iz Korotkoarmirovannykh Kompozitsionnykh Materialov [AnisoTopo Program for Constructing Anisotropic Stiffness Matrices of Elements in Problems of Topological Optimization of Structures from Short-Reinforced Composite Materials] 2021.
70. Armamid PA6 GF 50-1 TDS TDS Available online: https://polyplastic-compounds.ru/images/pdf/Armamid/ Armamid_PA6_GF_50-1.pdf (accessed on 19 October 2023).
71. Kurkin, E.; Spirina, M. Accuracy of the Short Fibers Reinforced Composite Material Plasticity Models. J Phys Conf Ser 2021, 12040, doi:10.1088/1742-6596/1925/1/012040.
72. Gamma Plast UPA 6 30 M TDS Available online: https://gamma-plast.ru/poliamid/uglenapolnenniy/poliamid-upa-6-30-m/ (accessed on 19 October 2023).
73. Kurkin, E.; Spirina, M.; Espinosa Barcenas, O.U.; Kurkina, E. Calibration of the PA6 Short-Fiber Reinforced Material Model for 10% to 30% Carbon Mass Fraction Mechanical Characteristic Prediction. Polymers (Basel) 2022, 14, doi:10.3390/polym14091781.
74. GOST 4784-97: Aluminium and wrought aluminium alloys. Grades
75. Plastics – Determination of Tensile Properties – Part 2: Test Conditions for Moulding and Extrusion Plastics; Geneva, CH, 2012; Vol. 2012;.
76. Komarov, V.; Kurkin, E.; Spirina, M.; Chertykovtseva, V. Multi-Level Computational-Experimental System For The Analysis Of Strength And Stiffness Of Elements Of Structures From Composites Reinforced By Short Fibers. Izvestiya of Samara Scientific Center of the Russian Academy of Sciences 2017, 6, 36–45.
77. Kurkin, E.I.; Kishov, E.A.; Lukyanov, O.E.; Espinosa Barcenas, O.U. Technique of Considering the Material Anisotropy in Topology Optimization of Short Fibers Composite Structures. In Proceedings of the Journal of Physics: Conference Series; IOP Publishing Ltd, June 21 2021; Vol. 1925.
78. Tandon, G. P.; Weng, G. J. The Effect of Aspect Ratio of Inclusions on the Elastic Properties of Unidirectionally Aligned Composites. Polymer Composites 1984, 5 (4), 327–333. https://doi.org/10.1002/pc.750050413.
79. Li, H.; Zare, Y.; Rhee, K. Y. Mathematical Simplification of the Tandon–Weng Approach to the Mori–Tanaka Model for Es-timating the Young's Modulus of Clay/Polymer Nanocomposites. JOM 2017, 69 (12), 2819–2824. https://doi.org/10.1007/s11837-017-2609-y.
80. Gusev, A. A. Finite Element Estimates of Viscoelastic Stiffness of Short Glass Fiber Reinforced Composites. Composite Struc-tures 2017, 171, 53–62. https://doi.org/10.1016/j.compstruct.2017.03.021.
81. Ghoreishi, S.N.; Clausen, A.; Joergensen, B.N. Termination Criteria in Evolutionary Algorithms: A Survey. In Proceedings of the IJCCI 2017 - Proceedings of the 9th International Joint Conference on Computational Intelligence; SciTePress, 2017; pp. 373–384.
82. Komarov, V.; Spirina, M.; Kurkin, E.; Kishov, E. Estimation of Weight Efficiency of Topologically Optimal Aerospace Structures;
83. Guest, J.K.; Lotfi, R.; Gaynor, A.T.; Jalalpour, M. Structural Topology Optimization: Moving Beyond Linear Elastic Structural Topology Optimization: Moving Beyond Linear Elastic Design Objectives Design Objectives Original Citation Original Citation "Structural Topology Optimization-Moving beyond Linear Elastic Design Objectives"; 2012.